
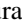



Element- and orbital-selective magnetic coherent rotation at the first-order phase transition of a hard uniaxial ferrimagnet

Sh. Yamamoto ^{1,*}, D. I. Gorbunov,¹ H. Akai ², H. Yasumura,³ Y. Kotani,⁴ T. Nakamura ^{3,4}, T. Kato,⁵ N. V. Mushnikov,⁶ A. V. Andreev,⁷ H. Nojiri,³ and J. Wosnitza^{1,8}

¹*Hochfeld-Magnetlabor Dresden (HLD-EMFL) and Würzburg-Dresden Cluster of Excellence ct.qmat, Helmholtz-Zentrum Dresden-Rossendorf, 01328 Dresden, Germany*

²*Institute for Solid State Physics, The University of Tokyo, Kashiwa, Chiba 277-8581, Japan*

³*Institute for Materials Research, Tohoku University, Sendai 980-8577, Japan*

⁴*Japan Synchrotron Radiation Research Institute, SPring-8, Sayo, Hyogo 679-5198, Japan*

⁵*Department of Electrical Engineering and Computer Science, Nagoya University, Nagoya 464-8603, Japan*

⁶*Institute of Metal Physics, Ural Branch of the Russian Academy of Sciences, Kovalevskaya 18, 620990 Ekaterinburg, Russia*

⁷*FZU Institute of Physics, Czech Academy of Sciences, 18221 Prague, Czech Republic*

⁸*Institut für Festkörper- und Materialphysik, TU Dresden, 01062 Dresden, Germany*



(Received 25 February 2020; revised manuscript received 20 April 2020; accepted 30 April 2020; published 19 May 2020)

$3d$ - $4f$ intermetallic compounds with heavy rare-earth elements show first-order phase transitions in high magnetic fields due to the competition between the exchange interaction and the magnetocrystalline anisotropy. However, the microscopic picture of the field-induced noncollinear magnetic structures remains elusive. Here we report the direct experimental observation of the coherent stepwise rotation of the $3d$ and $4f$ magnetic moments of the uniaxial hard ferrimagnet TmFe_5Al_7 by using soft x-ray magnetic circular dichroism in pulsed magnetic fields up to 25 T. The element- and shell-selective moments show a transition from the collinear ferrimagnet toward the forced ferromagnetic state via a canted phase, which is explained by a two-sublattice model.

DOI: [10.1103/PhysRevB.101.174430](https://doi.org/10.1103/PhysRevB.101.174430)

I. INTRODUCTION

Intermetallic compounds based on rare-earth (R) and transition-metal (T) elements have facilitated a wide range of technological developments for the past 50 years due to their good hard magnetic properties. The interplay between the itinerant $3d$ and the localized $4f$ electrons provides high magnetic-ordering temperature and high magnetocrystalline anisotropy, which are indispensable for permanent magnets [1]. In R - T systems with heavy rare-earth elements, the two-sublattice magnetizations couple ferrimagnetically in the ground state and show field-induced magnetic transitions by destabilizing the collinear antiparallel coupling under magnetic fields of tens of teslas [2]. The phase transitions originate from the local electronic correlations, such as intra and interatomic exchange and magneto-electric coupling, which involves crystal-field and spin-orbit interactions [3]. The element- and shell-selective magnetic and electronic information is of fundamental and technological interest. This information is needed for understanding the mechanism behind macroscopically observed field-induced phenomena.

Conventionally, high-field bulk magnetization has been used to extract phenomenological parameters of the inter-sublattice $3d$ - $4f$ exchange coupling and the magnetocrystalline anisotropy [2,4–8]. Basically, the field-induced phase

transition is expected to reflect simultaneous stepwise rotations of the R $4f$ and T $3d$ magnetic moments toward the forced ferromagnetic state where both sublattice moments point to the applied-field direction [9]. However, the direct observation of this conjectured processes was missing in R - T intermetallic compounds. This makes it challenging to extract the fundamental magnetic parameters of materials showing large field-induced noncollinearity of the R and T magnetic moments [10]. This limitation resulted from the lack of the proper probing technique in high magnetic fields beyond the static-field regime. Only recently, the field-induced modification of the magnetic structures has been indirectly reported for a strongly anisotropic ferrimagnet, HoFe_5Al_7 , from hard x-ray magnetic circular dichroism (XMCD) experiments at the Fe - K edge in pulsed magnetic fields [11]. However, the K -edge XMCD is composed of complicated contributions from multiple electronic orbitals both in the R and T sublattices. First, the Fe - K edge involves the dipole transition from $1s$ to $4p$ states and the XMCD signals mainly result from the spin-orbit splitting of the final p state due to the spherical symmetry of the initial s state [12–14]. Second, the intraatomic p - d interaction gives a finite contribution of the $3d$ electrons to the K -edge XMCD [13,14]. Third, there are also rare-earth influences, mainly from R $4f$ and $5d$ orbitals on the K -edge XMCD signals [15–17]. Therefore, in the hard x-ray regime, one needs to rely on a systematic comparison between R - T systems with magnetic and nonmagnetic R element [18,19], theory-based calculations [20–22], or mathematical procedures such as sin-

*s.yamamoto@hzdr.de

gular value decomposition [11,23] for estimating the element- and shell-selective information. On the other hand, XMCD in the soft x-ray regime can access directly the electronic $3d$ and $4f$ orbitals that govern the magnetic properties.

The aim of this work is to reveal directly the microscopic picture of the electronic properties and spin/orbital magnetic moments of the T $3d$ and the R $4f$ electrons during the field-induced magnetic phase transition for a hard uniaxial ferrimagnet. As a test example we chose TmFe_5Al_7 . The microscopic picture of the field-induced phase transition in the easy-axis system is expected to be essentially different from that of RFe_5Al_7 easy-plane systems, which show magnetic-moment rotations from one easy axis to another easy axis in the basal plane [11]. To achieve this goal, we performed soft x-ray absorption spectroscopy (XAS) and XMCD at the Tm $M_{4,5}$ ($3d_{3/2,5/2} \rightarrow 4f$) and the Fe $L_{2,3}$ ($2p_{1/2,3/2} \rightarrow 3d$) edges in pulsed magnetic fields up to 25 T. We observed pronounced variations of the XMCD spectra in the critical-field region. Complex magnetic states were revealed, from the collinear ferrimagnetic toward the forced-ferromagnetic state through a noncollinear canted-moment phase. Additionally, the field dependence of the element- and shell-selective spin and orbital moments were determined from the magneto-optical sum rules. Moreover, our microscopic data made it possible to simulate the magnetization process and extract the anisotropy constants of TmFe_5Al_7 .

TmFe_5Al_7 crystallizes in a tetragonal ThMn_{12} -type structure (see the Supplemental Material [24]) with Curie temperature of $T_C = 193$ K. Below 64 K, the uniaxial magnetocrystalline anisotropy of the Tm sublattice dominates the easy-plane anisotropy of the Fe sublattice leading to an easy-axis anisotropy. Thus, TmFe_5Al_7 represents the only case that shows easy-axis anisotropy in the RFe_5Al_7 family with heavy rare-earth elements. A field-induced first-order transition was observed at 10 to 15 T below 20 K by bulk magnetization and ultrasound measurements [25].

II. EXPERIMENTAL DETAILS

XAS and XMCD experiments in pulsed magnetic fields were performed at the twin-helical undulator beamline BL25SU in SPring-8 [26]. A pulsed magnet was used to generate magnetic fields along the [001] direction of the TmFe_5Al_7 single crystal. For 25 T pulses a charging voltage of 1.7 kV with a capacitance of 42.4 mF was used. The pulse width, which is defined by the time during which the magnetic field is larger than 10% of the maximum field, was 28 ms. Absorption signals were recorded in total-electron-yield (TEY) mode. Field-dependent TEY signals at each energy point were measured for both plus and minus helicities μ_+ and μ_- using a time-resolved acquisition technique with a sampling rate of 1 MHz [27]. The XAS and XMCD spectra were obtained from $(\mu_+ + \mu_-)/2$ and $\mu_+ - \mu_-$, respectively. The sample was cleaved under ultrahigh vacuum, at pressure below 2×10^{-7} Pa, to measure the absorption of the clean surface. All measurements in the current study were performed at 12 K.

III. RESULTS AND DISCUSSION

Figure 1 shows XAS data in zero field at the Tm $M_{4,5}$ and Fe $L_{2,3}$ edges. The spectral line shape has three components at

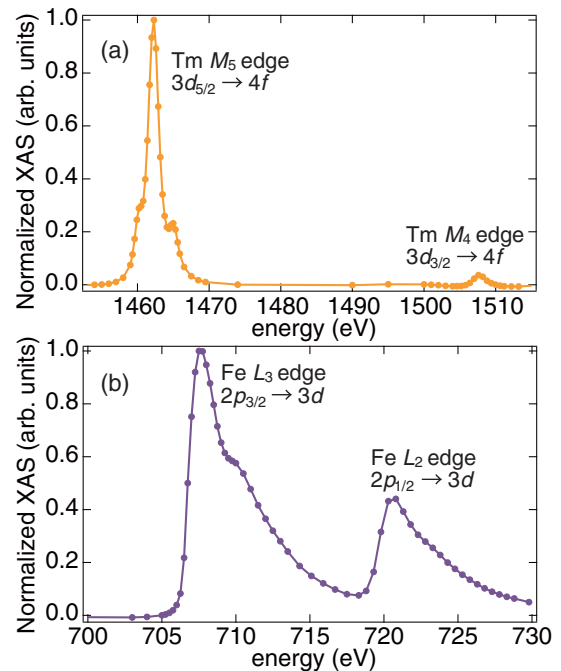


FIG. 1. X-ray absorption spectra (XAS) for a TmFe_5Al_7 single crystal at the (a) Tm $M_{4,5}$ and (b) the Fe $L_{2,3}$ edges in zero field at 12 K. The spectra were normalized to the absorption intensity at (a) 1462.3 and (b) 707.5 eV, respectively.

the M_5 edge and a single component at the M_4 edge [Fig. 1(a)]. These are typical trivalent absorption features for Tm [28]. Figure 1(b) shows two main peaks at 707.5 eV for the Fe L_3 edge and at 720.8 eV for the Fe L_2 edge. In addition, shoulder-like structures were observed at energies higher than the main peaks by $\simeq 2.5$ eV. Such shoulder structures remind us of Fe^{3+} that could have been created by oxidation during the beamtime [29]. Although surface oxidation after sample cleavage cannot be completely excluded, we confirmed that there was no detectable change of the spectral line shape recorded at the beginning and the end of the beamtime with respect to the position and intensity ratio between the main and the satellite peaks. The Fe atoms occupy two nonequivalent sites, $8f$ and $8j$, in the crystallographic unit cell. The Al atoms occupy the $8i$ site entirely and share the $8j$ site with Fe. Our first-principle calculations imply hybridization of the $8j$ -site Fe d and Al p states (see the Supplemental Material [24]), which possibly lead to these shoulder structures [30]. Further experiments of $3d$ - $4f$ systems with the same crystal structure without Al atom will provide further insights into this scenario.

Figures 2(a) and 2(b) show selected XMCD spectra recorded during the down sweep of a 25-T field pulse at the Tm $M_{4,5}$ and Fe $L_{2,3}$ edges, respectively. The spectral line shapes, both at the Tm M and the Fe L edges, do not change in the current field range and are in good agreement with earlier studies for Tm^{3+} [32] and metallic iron [33]. On the other hand, the XMCD amplitude shows a distinct evolution as function of magnetic field. The positive (negative) amplitudes at the Tm M_5 (Fe L_3) edge, which are observed in the spectra at low fields, are related to the magnetic moment of the Tm $4f$ (Fe $3d$) electrons that is antiparallel (parallel) to the field direction. This corresponds to the collinear ferrimagnetic

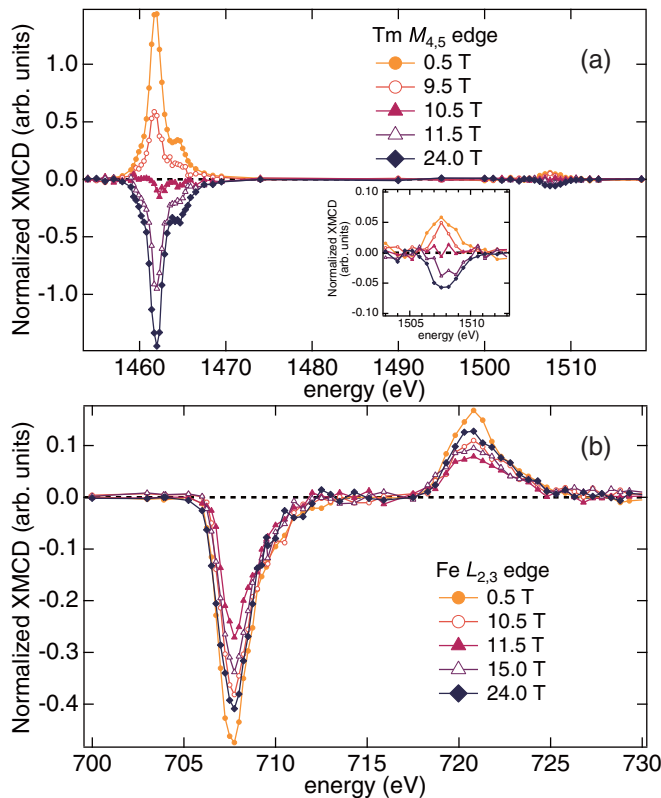


FIG. 2. X-ray magnetic circular dichroism (XMCD) spectra during the down sweep at the (a) Tm $M_{4,5}$ and (b) Fe $L_{2,3}$ edges in pulsed magnetic fields up to 24 T. The inset of (a) shows an enlarged view at the M_4 edge. All spectra are normalized to the (a) M_5 and (b) L_3 XAS peak intensity at each field.

order. In Fig. 2(a), with increasing field, the Tm M -edge MCD amplitude first reduces and changes its sign near 10 T. Subsequently, this negative peak grows along with the field. Figure 2(b) shows that the amplitudes of the Fe L_3 and L_2 edge decrease, reach a minimum near 10 T, and thereafter rise again. These variations of the MCD spectra evidence that the Tm $4f$ moments change their direction near 10 T and that the Fe $3d$ moments, initially, deviate from the field orientation, and then again align back to the original direction. Figure 3(a) shows the field dependence of the bulk magnetization and its field derivative along the [001] direction. This was recorded after applying a negative magnetic-field pulse, so that the initial state was single magnetic domain with negative spontaneous magnetization. This effect was considered by offsetting the pulsed-field data as shown in Fig. 3(a). A hysteric magnetization jump is observed in the critical-field region ranging from 9 to 12 T, which signals the known first-order field-induced transition [25]. The transition likely reflects a step-wise rotation of the Tm and Fe magnetic moments rather than a continuous paramagnetic remagnetization of the Tm moments as was found for $\text{Tm}_2\text{Co}_{17}$ [34]. In contrast to $\text{Tm}_2\text{Co}_{17}$, for TmFe_5Al_7 , the Tm moment does not rise to its full value at the phase transition and the transition shape does not show a strong temperature dependence [25]. The critical-field range agrees well with the fields where clear variations of the MCD spectra were observed in Figs. 2(a) and 2(b), which means that the surface region of a few nanometer thickness,

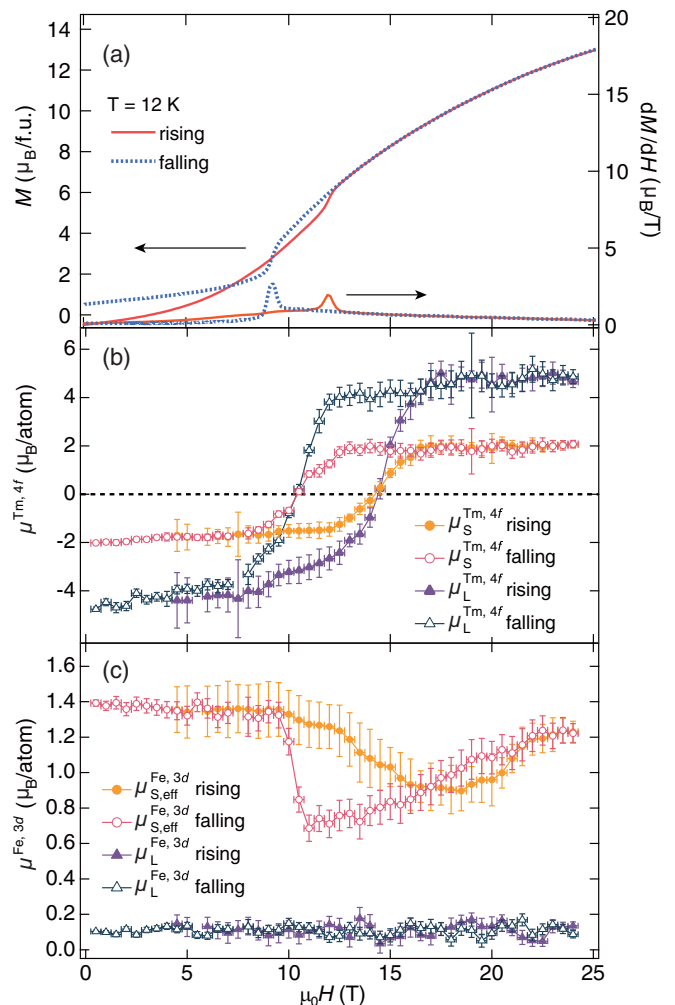


FIG. 3. (a) Bulk magnetization for field aligned along the [001] direction (left scale) and the field derivative (right scale) at 12 K. The solid (dashed) line corresponds to the up-sweep (down-sweep) result. Spin (circle) and orbital (triangle) magnetic moments projected along the [001] direction for the (b) Tm $4f$ and (c) Fe $3d$ electrons as a function of magnetic field. Filled (open) symbols were extracted from the spectra obtained during the up (down) sweep.

which is probed by the TEY mode in the XMCD experiments, has the same magnetic properties as the bulk single crystal.

To determine the spin and orbital magnetic moments of the Tm $4f$ and Fe $3d$ electrons, the magneto-optical sum rules [35,36] were applied to the XAS and XMCD spectra. They relate the spin and the orbital moments to the intensity integrals over respective XAS and XMCD spectra. Figures 3(b) and 3(c) show the orbital μ_L and spin μ_S magnetic moments carried by the Tm $4f$ and Fe $3d$ electrons as a function of the magnetic field. The Tm $4f$ spin moment $\mu_S^{\text{Tm},4f}$ was derived by taking into account the ratio between the ground-state expectation value of the magnetic dipole and the spin magnetic moment, $\langle T_z \rangle / \langle S_z \rangle$, which is 0.41, calculated for a free Tm^{3+} ion [37]. We also considered the correction coefficient for the jj mixing between the multiplet structure, $3d_{5/2}$ and $3d_{3/2}$, due to the $3d$ - $4f$ interaction [37]. The Fe $3d$ spin moment effectively includes the contribu-

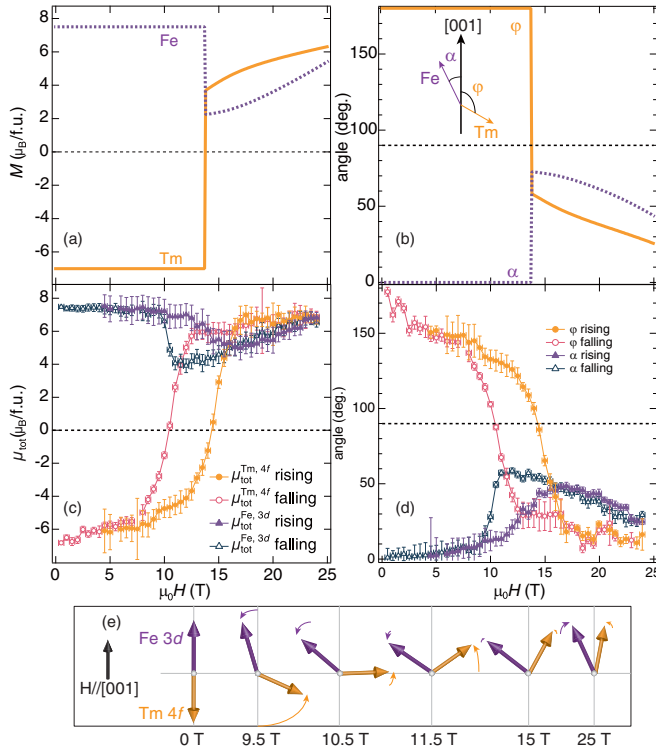


FIG. 4. Field dependence of the (a) Tm (solid line) and Fe (dashed line) sublattice magnetization and (b) the canting angle of the Tm (solid line) and Fe (dashed line) sublattice magnetization away from the [001] axis as shown in the inset simulated by the two-sublattice model. Field dependence of the (c) Tm (Fe) magnetic moment for the 4*f* (3*d*) electrons and (d) the canting angles extracted from (c). (e) A schematic diagram of the field-induced coherent rotation of the Tm 4*f* and the Fe 3*d* moments estimated from the data in (c) during the down sweep. The arrow lengths are scaled to the magnitude of the magnetic moment at 0 T.

tion from the magnetic dipole moment μ_T ($\mu_{S,\text{eff}}^{\text{Fe},3d} = \mu_S^{\text{Fe},3d} - 7\mu_L^{\text{Fe},3d}$). The hole numbers of the 4*f* and the 3*d* orbitals were assumed to be 2 [37], which is the value for a free Tm^{3+} ion, and 3.3 derived from the first-principle calculations (see the Supplemental Material [24]), respectively. The estimation of the experimental errors is described in the Supplemental Material [24]. The total moment for Tm 4*f* [(6.7 ± 0.1) μ_B/atom] and Fe 3*d* [(1.5 ± 0.1) μ_B/atom] obtained at 0.5 T is slightly smaller than the local moment derived from our calculation (7 μ_B/atom for Tm and 1.65 μ_B/atom for Fe). This underestimation of the magnetic moment of the order of 5 to 10% is typical for 3*d* and 4*f* metallic systems and presumably due to the intermixing of the multiplet structures [37,38]. It is worth noting that the Fe 3*d* moment estimated from the current experiment corresponds to the average moment of the Fe atoms at the 8*f* and 8*j* sites. Figure 3(b) shows that both the spin and orbital moments reverse their direction in the critical-field region. On the other hand, Fig. 3(c) reflects that for Fe 3*d* moment only the spin moment varies with respect to the field and the orbital part stays almost constant at a level of (0.1 ± 0.05) μ_B/atom , which is kept partially quenched by the crystal electric field within the current experimental resolution. These results mean that the localized 4*f* character

of the rare-earth metal determines the anisotropic magnetic behavior in this system. The XMCD amplitude also follows the same trend as the total moment with respect to magnetic field, which is shown in the Supplemental Material [24]. Figure 4(c) shows the field dependence of the total moment, which is given by the sum of the orbital and spin moment $\mu_{\text{tot}} = \mu_L + \mu_S$. From Figs. 3(b), 3(c), and 4(c), the following microscopic picture can explain the macroscopically observed first-order magnetic phase transition. First, below the critical-field range, the gradual increase in the bulk magnetization is dominated by the spin and the orbital moment of the Tm 4*f* electrons. Second, the magnetization jump in Fig. 3(a) mainly results from the spin-flop-like process of the Tm 4*f* moment. The coherent rotations of the Tm 4*f* and the Fe 3*d* moments expected during the field-induced phase transition are directly captured in the variation of each moment. The Fe moment starts to decrease along with the rotation of the Tm moment due to the antiferromagnetic coupling between the Tm and Fe sublattices. The peak in the field derivative of the magnetization [Fig. 3(a)] corresponds to the start (end) of the simultaneous coherent rotation of the Tm 4*f* and Fe 3*d* moments during the up (down) sweep. Third, above the critical-field range, the Tm spin and orbital moments are almost constant, therefore, the increase in this field range observed in the bulk magnetization is largely carried by the Fe 3*d* spin magnetic moment.

By use of a mean-field model, we simulate the field evolution of the total magnetization of TmFe_5Al_7 as well as of the individual Tm and Fe magnetic moments at 12 K. We consider a Hamiltonian based on the Tm-Fe intersublattice exchange interaction, magnetic anisotropy, and Zeeman energy. For each field value, we minimize the Hamiltonian with respect to the angles between the Tm and Fe magnetic moments and the applied field. Additional information can be found in the Supplemental Material [24]. For the anisotropy energy, we consider the uniaxial contribution of the Tm sublattice with anisotropy constants up to the sixth order, K_1^{Tm} , K_2^{Tm} , and K_3^{Tm} , following a standard approach [39], and a smaller planar contribution of the Fe sublattice with a second-order anisotropy constant, K_1^{Fe} :

$$E_a = K_1^{\text{Tm}} \sin^2 \phi + K_2^{\text{Tm}} \sin^4 \phi + K_3^{\text{Tm}} \sin^6 \phi + K_1^{\text{Fe}} \sin^2 \alpha, \quad (1)$$

where α and ϕ are defined by the angles between the Fe and Tm moments, respectively, and the [001] axis, as shown in the inset of Fig. 4(b). $K_1^{\text{Fe}} \simeq -1.2 \text{ MJ/m}^3$ was taken from the magnetization data for LuFe_5Al_7 with nonmagnetic Lu [40]. Figure 4 shows the best fit to the macro and microscopic experimental data. The canting angle in Fig. 4(d) is extracted from the simple formula $\cos \theta = \mu_{\text{tot}}(H)/|\mu_{\text{tot}}(0)|$ ($\theta = \alpha$ or ϕ). The schematic diagram of the coherent rotation is depicted in Fig. 4(e). The anisotropy constants $K_1^{\text{Tm}} = 2.46 \pm 0.2 \text{ MJ/m}^3$, $K_2^{\text{Tm}} = -1.60 \pm 0.2 \text{ MJ/m}^3$, and $K_3^{\text{Tm}} \simeq 0$. K_1^{Tm} were found by adjusting the height of the magnetization jump at the transition as well as the saturation field, $\sim 30 \text{ T}$ [25]. For $K_2^{\text{Tm}} > 0$, we did not observe any changes in the magnetization process, whereas negative K_2^{Tm} improved the M_{Fe} jump. For larger K_2^{Tm} , a second field-induced transition appears, which is at variance with the experiment. Any value of K_3^{Tm} other than zero reduced the quality of the fit either

through an increase of the M^{Fe} jump or the emergence of an additional transition. The experimental data in Fig. 4(c) show the finite susceptibility before the field-induced phase transition (below 10 T) especially for $\mu_{\text{tot}}^{\text{Tm}}$, which reflects the relatively weak exchange interaction between the Tm and the Fe sublattice [11].

IV. CONCLUSION

In summary, we investigated the element- and orbital-selective magnetic coherent rotation during the field-induced magnetic phase transition of the uniaxial hard ferrimagnet TmFe_5Al_7 by using soft-x-ray magnetic circular dichroism in pulsed-magnetic fields up to 25 T. Noncollinear magnetic states in high magnetic fields, composed of the Tm $4f$ and Fe $3d$ spin and orbital magnetic moments, were unambiguously determined, which gives a direct microscopic picture of the field-induced magnetic phase transition. From a methodological point of view, pulsed-field soft x-ray MCD spectroscopy, which gives absolute spin and orbital moments along the field direction, complements pulsed-field neutron scattering for studying field-induced noncollinear magnetic structures that

are central topics in frustrated, multiferroic, and spintronic systems as well as potential materials for permanent magnets.

ACKNOWLEDGMENTS

We acknowledge support of the HLD at HZDR, member of the European Magnetic Field Laboratory (EMFL) and from the DFG through the Würzburg-Dresden Cluster of Excellence on Complexity and Topology in Quantum Matter–*ct.qmat* (EXC 2147, Project-No. 39085490). The synchrotron radiation experiments were performed at the BL25SU of SPring-8 with the approval of the Japan Synchrotron Radiation Research Institute (JASRI) (Proposal No. 2018B1197). The work was supported by Project No. 19-00925S of the Czech Science Foundation and by Materials Growth, Measurements Laboratory within the Program of Czech Research Infrastructures (Project No. LM2018096) and Russian Foundation for Basic Research (Grant No. 18-02-00294). A part of this work was supported by Nagoya University microstructural characterization platform as a program of “Nanotechnology Platform” of the Ministry of Education, Culture, Sports, Science, and Technology (MEXT), Japan. H.N. acknowledges support by KAKENHI 18H04300.

-
- [1] R. Skomski and J. M. D. Coey, *Permanent Magnetism* (CRC Press, Boca Raton, FL, 1999).
- [2] A. K. Zvezdin, in *Handbook of Magnetic Materials*, Vol. 9, edited by K. H. J. Buschow, (Elsevier, Amsterdam, 1995), p. 405.
- [3] J. J. M. Franse, F. E. Kayzel, and N. P. Thuy, Exchange and anisotropy in 3d-4f compounds, *J. Magn. Magn. Mater.* **129**, 26 (1994).
- [4] H. Kato, D. W. Lim, M. Yamada, Y. Nakagawa, H. A. Katori, and T. Goto, Field-induced phase transitions in ferrimagnetic $\text{R}_2\text{Fe}_{14}\text{B}$ in ultra-high magnetic fields, *Physica B* **211**, 105 (1995).
- [5] B. Garcia-Landa, P. A. Algarabel, M. R. Ibarra, F. E. Kayzel, and J. J. M. Franse, Analysis of the intrinsic magnetic properties of R_2Fe_{17} single crystals (R= Y, Dy, Ho, Er), *Phys. Rev. B* **55**, 8313 (1997).
- [6] Y. Skourski, M. D. Kuz'min, K. P. Skokov, A. V. Andreev, and J. Wosnitza, High-field magnetization of $\text{Ho}_2\text{Fe}_{17}$, *Phys. Rev. B* **83**, 214420 (2011).
- [7] N. V. Kostyuchenko, A. K. Zvezdin, E. A. Tereshina, Y. Skourski, M. Doerr, H. Drulis, I. A. Pelevin, and I. S. Tereshina, High-field magnetic behavior and forced-ferromagnetic state in an $\text{ErFe}_{11}\text{TiH}$ single crystal, *Phys. Rev. B* **92**, 104423 (2015).
- [8] I. S. Tereshina, N. V. Kostyuchenko, E. A. Tereshina-Chitrova, Y. Skourski, M. Doerr, I. A. Pelevin, A. K. Zvezdin, M. Paukov, L. Havela, and H. Drulis, ThMn_{12} -type phases for magnets with low rare-earth content: Crystal-field analysis of the full magnetization process, *Sci. Rep.* **8**, 3595 (2018).
- [9] D. I. Gorbunov, S. Yasin, A. V. Andreev, Y. Skourski, N. V. Mushnikov, E. V. Rosenfeld, S. Zherlitsyn, and J. Wosnitza, Magnetic anisotropy and magnetic phase transitions in RFe_5Al_7 , *J. Magn. Magn. Mater.* **383**, 208 (2015).
- [10] A. Sarkis and E. Callen, Magnetic anisotropy of rare-earth-transition-metal compounds, *Phys. Rev. B* **26**, 3870 (1982).
- [11] D. I. Gorbunov, C. Strohm, M. S. Henriques, P. van der Linden, B. Pedersen, N. V. Mushnikov, E. V. Rosenfeld, V. Petříček, O. Mathon, J. Wosnitza, and A. V. Andreev, Microscopic Nature of the First-Order Field-Induced Phase Transition in the Strongly Anisotropic Ferrimagnet HoFe_5Al_7 , *Phys. Rev. Lett.* **122**, 127205 (2019).
- [12] J. Herrero-Albillos, D. Paudyal, F. Bartolomé, L. M. García, V. K. Pecharsky, K. A. Gschneidner Jr, A. T. Young, N. Jaouen, and A. Rogalev, Interplay between Er and Co magnetism in ErCo_2 , *J. Appl. Phys.* **103**, 07E146 (2008).
- [13] J. Igarashi and K. Hirai, Magnetic circular dichroism at the K edge of nickel and iron, *Phys. Rev. B* **50**, 17820 (1994).
- [14] J. Igarashi and K. Hirai, Orbital moment and magnetic circular dichroism at the K edge in ferromagnetic cobalt, *Phys. Rev. B* **53**, 6442 (1996).
- [15] J. Chaboy, H. Maruyama, L. M. García, J. Bartolomé, K. Kobayashi, N. Kawamura, A. Marcelli, and L. Bozukov, X-ray magnetic circular dichroism at the iron K edge in rare-earth-transition-metal intermetallics: Experimental probe of the rare-earth magnetic moment, *Phys. Rev. B* **54**, R15637 (1996).
- [16] M. A. Laguna-Marco, J. Chaboy, and H. Maruyama, Element-selective thermal x-ray magnetic circular dichroism study through the magnetic compensation temperature of $\text{Ho}_6\text{Fe}_{23}$, *Phys. Rev. B* **72**, 094408 (2005).
- [17] R. Boada, C. Piquer, M. A. Laguna-Marco, and J. Chaboy, Additivity of magnetic contributions to the x-ray magnetic circular dichroism spectrum, *Phys. Rev. B* **81**, 100404 (2010).
- [18] J. Chaboy, C. Piquer, N. Plugaru, F. Bartolomé, M. A. Laguna-Marco, and F. Plazaola, ^{57}Fe Mössbauer and x-ray magnetic circular dichroism study of magnetic compensation of the rare-

- earth sublattice in $\text{Nd}_{2-x}\text{Ho}_x\text{Fe}_{14}\text{B}$ compounds, *Phys. Rev. B* **76**, 134408 (2007).
- [19] M. A. Laguna-Marco, J. Chaboy, C. Piquer, H. Maruyama, N. Ishimatsu, N. Kawamura, M. Takagaki, and M. Suzuki, Revealing Fe magnetism in lanthanide-iron intermetallic compounds by tuning the rare-earth $L_{2,3}$ -edge x-ray absorption edges, *Phys. Rev. B* **72**, 052412 (2005).
- [20] H. Ebert, P. Strange, and B. L. Gyorffy, Theory of circularly polarized x-ray absorption by ferromagnetic Fe, *J. Appl. Phys.* **63**, 3055 (1988).
- [21] C. Brouder and M. Hikam, Multiple-scattering theory of magnetic x-ray circular dichroism, *Phys. Rev. B* **43**, 3809 (1991).
- [22] A. L. Ankudinov and J. J. Rehr, Relativistic calculations of spin-dependent x-ray-absorption spectra, *Phys. Rev. B* **56**, R1712 (1997).
- [23] C. Strohm, P. van der Linden, O. Mathon, and S. Pascarelli, Simultaneous Observation of the Er-and Fe-Sublattice Magnetization of Ferrimagnetic $\text{Er}_3\text{Fe}_5\text{O}_{12}$ in High Magnetic Fields Using X-Ray Magnetic Circular Dichroism at the Er $L_{2,3}$ Edges, *Phys. Rev. Lett.* **122**, 127204 (2019).
- [24] See Supplemental Material at <http://link.aps.org/supplemental/10.1103/PhysRevB.101.174430> for the crystal structure, the time structure of the pulsed magnetic field, the estimation of the experimental errors, the first-principle calculations, details of the mean-field model, and the comparison between the XMCD amplitude and the total-magnetic moment, which includes Refs [25], [31], and [40–42].
- [25] D. I. Gorbunov, S. Yasin, A. V. Andreev, N. V. Mushnikov, E. V. Rosenfeld, Y. Skourski, S. Zherlitsyn, and J. Wosnitza, Phase transitions of anisotropic and exchange origins in TmFe_5Al_7 , *Phys. Rev. B* **89**, 214417 (2014).
- [26] Y. Senba *et al.*, Upgrade of beamline BL25SU for soft x-ray imaging and spectroscopy of solid using nano- and micro-focused beams at SPring-8, *AIP Conf. Proc.* **1741**, 030044 (2016).
- [27] T. Nakamura *et al.*, Soft X-ray magnetic circular dichroism of a CoFe/MnIr exchange bias film under pulsed high magnetic field, *Appl. Phys. Express* **4**, 066602 (2011).
- [28] J. B. Goedkoop, B. T. Thole, G. van der Laan, G. A. Sawatzky, F. M. F. de Groot, and J. C. Fuggle, Calculations of magnetic x-ray dichroism in the 3d absorption spectra of rare-earth compounds, *Phys. Rev. B* **37**, 2086 (1988).
- [29] H. Suzuki, A. Nambu, and M. Okamoto, X-ray magnetic circular dichroism and neutron diffraction measurements of the magnetic moment of titanium in $\text{Sm}(\text{Fe}_{0.8}\text{Co}_{0.2})_{11}\text{Ti}$, *Phys. Rev. B* **100**, 144443 (2019).
- [30] K. Ito, K. Toko, Y. Takeda, Y. Saitoh, T. Oguchi, T. Suemasu, and A. Kimura, Local electronic states of Fe_4N films revealed by x-ray absorption spectroscopy and x-ray magnetic circular dichroism, *J. Appl. Phys.* **117**, 193906 (2015).
- [31] L. D. Finkelstein, A. V. Efremov, M. A. Korotin, A. V. Andreev, D. I. Gorbunov, N. V. Mushnikov, I. S. Zhidkov, A. I. Kukhareenko, S. O. Cholakh, and E. Z. Kurmaev, XPS spectra, electronic structure, and magnetic properties of RFe_5Al_7 intermetallics, *J. Alloys Compd.* **733**, 82 (2018).
- [32] A. Quindeau *et al.*, $\text{Tm}_3\text{Fe}_5\text{O}_{12}/\text{Pt}$ heterostructures with perpendicular magnetic anisotropy for spintronic applications, *Adv. Electron. Mater.* **3**, 1600376 (2017).
- [33] C. T. Chen, Y. U. Idzerda, H.-J. Lin, N. V. Smith, G. Meigs, E. Chaban, G. H. Ho, E. Pellegrin, and F. Sette, Experimental Confirmation of the X-Ray Magnetic Circular Dichroism Sum Rules for Iron and Cobalt, *Phys. Rev. Lett.* **75**, 152 (1995).
- [34] A. V. Andreev, M. D. Kuz'Min, Y. Narumi, Y. Skourski, N. V. Kudrevatykh, K. Kindo, F. R. de Boer, and J. Wosnitza, High-field magnetization study of a $\text{Tm}_2\text{Co}_{17}$ single crystal, *Phys. Rev. B* **81**, 134429 (2010).
- [35] B. T. Thole, P. Carra, F. Sette, and G. van der Laan, X-Ray Circular Dichroism as a Probe of Orbital Magnetization, *Phys. Rev. Lett.* **68**, 1943 (1992).
- [36] P. Carra, B. T. Thole, M. Altarelli, and X. Wang, X-Ray Circular Dichroism and Local Magnetic Fields, *Phys. Rev. Lett.* **70**, 694 (1993).
- [37] Y. Teramura, A. Tanaka, B. T. Thole, and T. Jo, Effect of coulomb interaction on the X-ray magnetic circular dichroism spin sum rule in rare earths, *J. Phys. Soc. Jpn.* **65**, 3056 (1996).
- [38] C. Piamonteze, P. Miedema, and F. M. F. De Groot, Accuracy of the spin sum rule in XMCD for the transition-metal L edges from manganese to copper, *Phys. Rev. B* **80**, 184410 (2009).
- [39] J. J. M. Franse and R. J. Radwański, in *Handbook of Magnetic Materials*, Vol. 7, edited by K. H. J. Buschow, (Elsevier, Amsterdam, 1993), p. 307.
- [40] D. I. Gorbunov, A. V. Andreev, S. Daniš, and J. Pospíšil, Evolution of magnetism in $\text{LuFe}_x\text{Al}_{12-x}$ ($4 \leq x \leq 6$) single crystals, *J. Alloys Compd.* **563**, 63 (2013).
- [41] H. Akai, Fast Korringa-Kohn-Rostoker coherent potential approximation and its application to FCC Ni-Fe systems, *J. Phys.: Condens. Matter* **1**, 8045 (1989).
- [42] M. T. Hutchings, Point-charge calculations of energy levels of magnetic ions in crystalline electric fields, *Solid State Phys.* **16**, 227 (1964).